RSC Advances

PAPER

Cite this: *RSC Adv.*, 2015, **5**, 61631

3D hierarchical Co_3O_4 microspheres with enhanced lithium-ion battery performance†

Zichao Zhang,[a] Li Li,*[ab] Qi Xu[a] and Bingqiang Cao*[a]

Received 16th June 2015
Accepted 10th July 2015

DOI: 10.1039/c5ra11472a

www.rsc.org/advances

Although transition metal oxide electrodes have large lithium storage capacity, they often suffer from low rate capability and poor cycling stability. To develop an electrode with a long cycle life and good rate capability, 3D hierarchical tricobalt tetraoxide (Co_3O_4) spheres are fabricated under various hydrothermal conditions and evaluated as an anode in lithium-ion batteries. 3D hierarchical urchin-like Co_3O_4 electrodes exhibit a high reversible discharge capacity, excellent rate capability and good cycling performance, owing to their hierarchical architecture composed of micro-/nanostructures. Electrochemical testing shows that stable reversible capabilities of 1228 and 820 mA h g^{-1} can still be maintained after 170 cycles at 200 and 500 mA g^{-1}, respectively. After rate capacity performance measurements, even the current density is increased to 3200 mA g^{-1} and a capacity of 587 mA h g^{-1} is retained after 500 cycles. The unique 3D hierarchical urchin-like Co_3O_4 electrode facilitates lithium ion diffusion and electron transportation and mitigates the internal mechanical stress induced by the volume variations of the electrode upon cycling, which lead to outstanding electrochemical performance.

1. Introduction

Many green and renewable power sources like water, wind, and solar energy are becoming research hotspots. In order to cope with their intermittence and meet the demand for mobile power, lithium-ion batteries (LIBs) are one of the most promising energy storage systems.[1] The electrode material, one of the key components of the LIBs, determines whether LIBs can fully display their advantages or not.[2] Nevertheless, the most widely used anode material for commercial LIBs, graphite, only hosts a theoretical capacity of 372 mA h g^{-1}.[3] To overcome this limitation, it is currently an urgent task to explore novel anode materials with high capacity and excellent rate capability.[4,5]

In contrast to the intercalation reaction mechanism of graphite, transition metal oxides (TMOs) can interact with lithium based on the conversion mechanism ($MO_x + 2xLi \leftrightarrow M + xLi_2O$).[6–8] TMO_x can store more lithium atoms and deliver multiple electrons in the redox reaction process.[9–14] Among various TMOs, Co_3O_4 has attracted extensive interest due to its high lithium-storage of about 890 mA h g^{-1}.[15–18] However, Co_3O_4 electrode still suffers from inferior cyclability and poor rate capability caused by the large volume expansion during the charge–discharge process and the lack of electrically conductive pathways. To address these challenges, nanometer-scale Co_3O_4 structures with diverse morphologies have been synthesized through a variety of methods. Pioneering works demonstrated that the controlled nanostructured Co_3O_4 electrodes could effectively enhance specific capacity, long-term cycling stability and rate performance.[19–25] Thus, various Co_3O_4 nanomaterials with interesting architectures, such as nanoparticles,[20] nanorods,[21] nanotubes,[22] nanoplates,[23] nanocages[24] and nanoflowers[25] have been designed and tested to restrain the large volume changes. However, Co_3O_4 is cubic and lacks structural anisotropy for one-dimensional (1D) or two-dimensional (2D) growth.[26] Fortunately, Co_3O_4 with a designed structure and morphology can be synthesized through the way of a morphology-conserved transformation from its precursor. For instance, Zhan *et al.* synthesized porous Co_3O_4 nanosheets through controlling thermal oxidative decomposition and recrystallization of hexagonal $Co(OH)_2$ nanosheets precursor.[27] Chen *et al.* reported different cobalt-based nanostructures and found that Co_3O_4 nanoflowers showed the best cycling performance (649 mA h g^{-1} after 100 cycles), compared to nanocubes and nanodiscs.[28] Wang *et al.* prepared self-stacked Co_3O_4 nanosheets from the cobalt acetate precursors and obtained a capacity of 1070 mA h g^{-1} at a current density of 178 mA g^{-1}.[29] Yan *et al.* prepared Co_3O_4 with opened-book morphology, which showed a high specific capacity (597 mA h g^{-1} after 50 cycles at a current density of 800 mA g^{-1}) and excellent rate capability.[30]

As efficient and effective transportation of lithium ions and electrons is considered as the key factor for improving the rate capability and long-term cycling stability, Co_3O_4 nanomaterials with three-dimensional (3D) hierarchical framework are one of

[a]*Key Laboratory of Inorganic Functional Materials in Universities of Shandong, School of Materials Science and Engineering, University of Jinan, Jinan 250022, China. E-mail: mse_lil@ujn.edu.cn; mse_caobq@ujn.edu.cn*

[b]*Key Laboratory of Advanced Energy Materials Chemistry (Ministry of Education), Nankai University, Tianjin 300071, China*

† Electronic supplementary information (ESI) available. See DOI: 10.1039/c5ra11472a

the most promising structures when used as anode material in LIBs. The shortened lithium ion diffusion pathway and large surface area provided by 3D hierarchical structures can facilitate ion transport and enable access to a large number of lithium ions. Furthermore, the large cavities among the nano-sized particles of the 3D frameworks can alleviate volume strain and stabilize the structure during the intercalation–deintercalation processes.[31,32] Most importantly, the more conductive 3D network structures can transfer electrons in a timely way that significantly reduce the polarization and enhance the rate capability. However, most of the above 3D hierarchical structures of Co_3O_4 were multi-step synthesized and costly due to the use of templates.[33]

In this paper, we fabricated 3D hierarchical Co_3O_4 materials *via* a simple hydrothermal method, subsequently thermal annealing in air and then used as anode for LIBs. In addition, we also systematically investigated the growth mechanism of 3D hierarchical Co_3O_4 spheres by controlling the hydrothermal reaction time and the effects of reaction conditions on material morphologies and dimensions. As expected, 3D hierarchical urchin-like Co_3O_4 electrode exhibits high lithium-storage capacity and impressive rate capability, owing to the unique hierarchical architecture with high electrode–electrolyte contact area, fast lithium ion diffusion and good strain accommodation. When cycled at the current densities of 200, 400, 800, 1400, 2200 and 3200 mA g^{-1}, this electrode delivers discharge capacities of 1158, 1195, 1223, 1184, 1077 and 906 mA h g^{-1}, respectively. Importantly, after rate capacity performance measurements, even the current density is increased to 3200 mA g^{-1}, a capacity of 587 mA h g^{-1} is retained after 500 cycles, indicating the potential application of 3D hierarchical urchin-like Co_3O_4 as anode materials for LIBs.

2. Experimental section

2.1 Materials synthesis

The 3D hierarchical Co_3O_4 spheres were fabricated by a thermal annealing-induced phase transformation from a morphology-similar precursor synthesized by hydrothermal method. All the reagents used were AR grade and were not purified further. DI water was used throughout the experiment. Firstly, cobalt nitrate hexahydrate and sodium chloride were dissolved in water, and then 12.5 mL urea aqueous solution was added in the above mixed solution under stirring to obtain pink precursor solution. The as-prepared mixed solution was transferred into a 50 ml Teflon-lined stainless steel autoclave and kept at 150 °C for different time after sealed. The light pink flocculent precipitates were collected by centrifugation and dried at 80 °C oven for 12 h after rinsing several times with distilled water and ethanol. The gray-black final products were produced by heating as-prepared light pink flocculent precipitates in air at 350 °C for 2 h with a ramping rate of 2 °C min^{-1}.

2.2 Materials characterizations

The crystal structure and phase of as-prepared products were characterized with X-ray powder diffraction (XRD; BRUKER-AXS, D8 ADVANCE, filtered Cu Kα radiation $\lambda = 0.1542$ nm, at 40 kV and 100 mA). Raman spectra were collected on a Thermo Scientific Raman Microscope DXR with 532 nm laser excitation at room temperature. The morphologies and microstructures of the products were examined by a field-emission scanning electron microscope (FESEM; FEI, Quanta FEG 250, operated at 10 kV) and a high-resolution transmission electron microscope (HRTEM; JEOL, JEM-2100, 200 kV, with electron diffraction). The nitrogen adsorption and desorption isotherms were measured on a Quantachrome ASIQC-4 instrument at 77 K with the samples outgassed at 150 °C for 0.5 h under vacuum before measurements. Thermal gravimetric analysis (TGA) was carried out on samples placed in corundum crucibles with a heating rate of 5 °C min^{-1} (TGA/DSC 1; METTLER).

2.3 Electrochemical measurements

The electrochemical tests were performed using a coin-type half cell (CR 2025). Metallic lithium was used as the counter/reference electrode and a polypropylene microporous membrane (Celgard 2400) was used as the separator. The Co_3O_4 anode disc was fabricated by cutting coated Cu foil using a compact and precision disc cutter (MSK-T-10, MTI Corporation). To prepare working electrodes, Co_3O_4 powders, conductivity agent (acetylene black, Super P®) and sodium carboxymethyl cellulose (CMC) with mass ratio 80 : 10 : 10 were mixed into a homogeneous slurry in deionized water with a pestle and mortar. The slurry mixture was coated onto Cu foil and then dried at 80 °C for 12 h under vacuum. The electrolyte was composed of 1 mol L^{-1} $LiPF_6$–ethylene carbonate (EC)–dimethyl carbonate (DMC)–ethylmethyl carbonate (EMC) (1 : 1 : 1 by volume). Coin cells were assembled using a compact hydraulic crimping machine (MSK-110, MTI Corporation) in an argon-filled glove-box (Universal 2400/750/900, MIKROUNA) with oxygen and water lower than 0.1 ppm. The galvanostatic charge–discharge tests of 3D hierarchical microsphere Co_3O_4 were carried out using a battery testing system LAND CT2001 (Wuhan LAND electronics, China) with a cutoff voltage range from 0.01 V to 3.0 V (*vs.* Li^+/Li) and current densities between 200 mA g^{-1} and 3200 mA g^{-1}. Cyclic voltammetry (CV) was performed on a Zahner/Zennium electrochemical workstation in the potential range 0.01–3.0 V (*vs.* Li^+/Li) at a scanning rate of 0.1 mV s^{-1} at room temperature. For the electrochemical impedance spectroscopy (EIS) measurements, the excitation voltage applied to the cell was 5 mV and the frequency range was from 100 kHz to 0.01 Hz.

3. Results and discussion

The morphologies and dimensions of the as-prepared cobalt-based precursors (CP) are first characterized with FE-SEM. The hydrothermal reaction time, solution molar ratio and the concentration of Co^{2+} all affect the formation of the final Co_3O_4 structures. The morphology controllability of precursor can be realized through changing hydrothermal time. By optimizing the hydrothermal reaction condition, Co_3O_4 nanoparticles, nanorods and the hierarchical spheres have been synthesized

(Fig. 1 and Fig. S1†). Fig. 1 shows FE-SEM images of the as-prepared precursors with typical structure. Herein, the three kinds of spheres with different morphologies are obtained under different hydrothermal time, as illustrated in Fig. 1a–c. The cobalt-based precursors (CP) are simply named CP-A, CP-B and CP-C, according to 0.5 h, 1 h and 6 h hydrothermal treatment, respectively. Fig. S2† displays the XRD pattern of the CP-C, which can be indexed to $Co(CO_3)_{0.5}(OH)\cdot 0.11H_2O$ (JCPDS card no. 048-0083).[34] The CP-A spheres with diameter ranging from 8 μm to 16 μm (Fig. 1a) are composed of lots of nanorods which gather in a centre. The hydrothermal time plays a crucial role in the formation of the 3D hierarchical spheres with different morphologies. At 0.5 h, the fuzzy spheres are formed with few nanorods. After 1 h, nanorods on the sphere seem to be more dense and spherical shape becomes more obvious. When the reaction time is extended to 6 h, nanorods grow to be thicker and the spherical structure is maintained. Generally, crystal growth of nanomaterial is modulated in accordance with the selective adsorption of the solvents, inorganic additives and precipitants to certain crystallographic planes. The selective adsorption based on the surface energy determines the growth of the crystal planes leading to a specific shape of the material.[35] Sodium chloride involves in the reaction between $Co(NO_3)_2\cdot 6H_2O$ and urea to form the hierarchical spheres.

The thermal decomposition behavior of the precursor was analyzed by thermal gravimetric analysis (TGA). The test was performed in air. Fig. S3† displays a TG curve of CP-C. It can be seen that the initial weight loss takes place at 280 °C is mainly attributed to the removal of physically adsorbed water and partial decomposition of the precursor into Co_3O_4, CO_2 and H_2O in the presence of oxygen during the measurement. The abrupt change in weight occurs at a temperature of 320 °C, suggesting the conversion from precursor to Co_3O_4. No obvious weight loss of precursor is found after 350 °C, suggesting the complete conversion from precursors to Co_3O_4. High temperature may lead to the collapse of the 3D hierarchical structure. Therefore, the calcination temperature for Co_3O_4 preparation is set at 350 °C in this study. The phase composition and structure of products were then investigated by X-ray diffraction (XRD), as shown in Fig. 2a. The diffraction peaks at 19°, 31.3°, 36.8°, 44.8°, 55.65°, 59.4°, 65.2°, 77.34° can be perfectly indexed to Co_3O_4 (111), (220), (311), (400), (422), (511), (440), (533) planes of cubic structure (PDF card: 42-1467), respectively. It reveals the complete conversion to Co_3O_4 after calcination. The Raman spectrum of the products was measured at room temperature. Fig. 2b displays four bands located at 466, 508, 601, and 669 cm^{-1}, corresponding to the E_g, F_{2g}, F_{2g}, and A_{1g} modes of the spinel Co_3O_4 phase, respectively.[36] The Raman spectrum further demonstrates the as-synthesized product is pure cobalt oxide without any impurities.

After cobalt-based precursors are annealed at 350 °C in air, the FE-SEM images of the as-prepared products are depicted in Fig. 3a–c. The as-synthesized metal oxides are simply named Co_3O_4-A, Co_3O_4-B and Co_3O_4-C, respectively. The morphologies and dimensions of Co_3O_4 are almost identical to those of their precursors. The 3D Co_3O_4 spheres are composed of lots of nanorods. The FE-SEM image also shows that the nanorods grow outward from the core and become hyper-branched. For as-obtained Co_3O_4-A, the growth of the nanorods is not uniform and not unidirectional. The porous between the nanorods in Co_3O_4-B is smaller than Co_3O_4-C. Co_3O_4-C spheres have the urchin-like shape. From FE-SEM image of Co_3O_4-C (Fig. 3c), nanorods connect with each other and gather together at the top of them. Fig. 3d–f show the corresponding magnified SEM images of nanorods, in which each nanorod is composed of

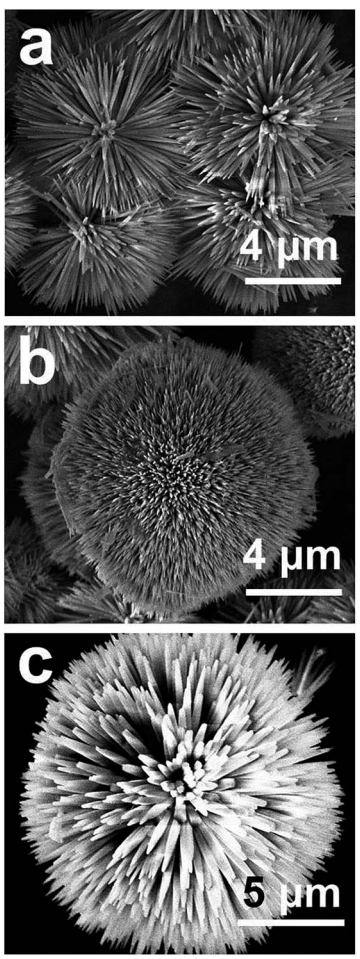

Fig. 1 SEM images of the Co_3O_4 precursors synthesized at 150 °C for different hydrothermal reaction times: (a) CP-A, 0.5 h; (b) CP-B, 1 h; (c) CP-C, 6 h.

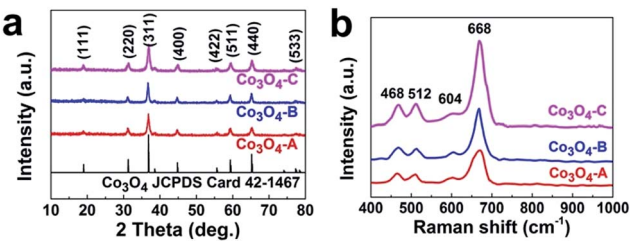

Fig. 2 (a) XRD patterns of Co_3O_4-A, Co_3O_4-B, Co_3O_4-C and standard of Co_3O_4 from JCPDS card 42-1467; (b) Raman spectrum of Co_3O_4-A, Co_3O_4-B, Co_3O_4-C.

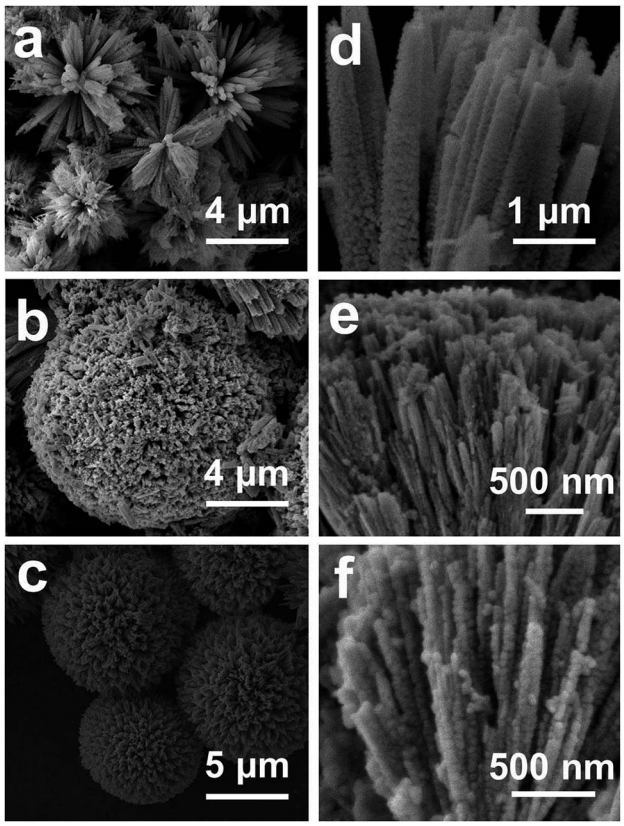

Fig. 3 SEM images of the urchin-like Co_3O_4 at different resolutions: (a and d) Co_3O_4-A; (b and e) Co_3O_4-B and (c and f) Co_3O_4-C.

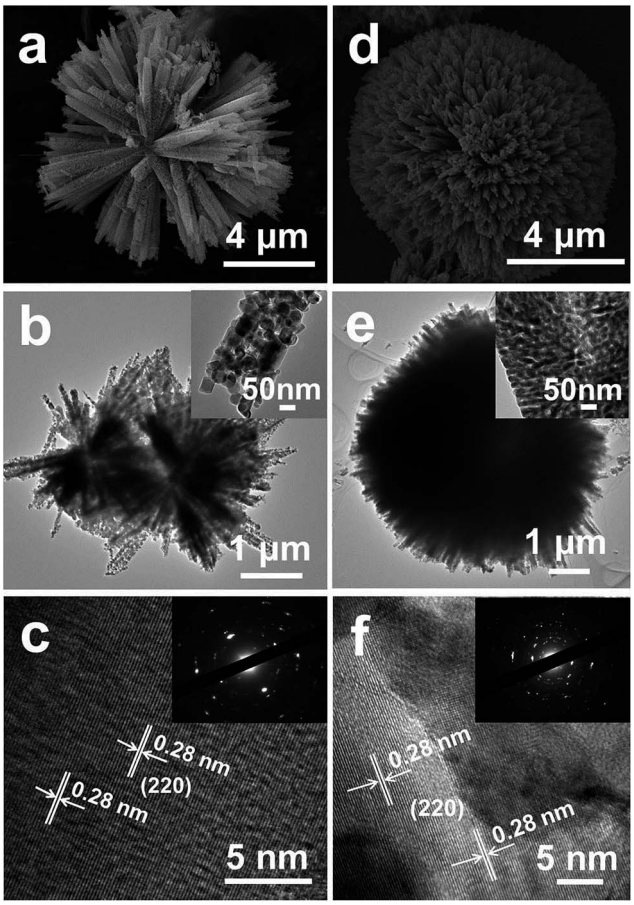

Fig. 4 SEM images of (a) Co_3O_4-A and (d) Co_3O_4-C; TEM images of (b) Co_3O_4-A and (e) Co_3O_4-C; HR-TEM images and the corresponding SAED patterns (insets) of (c) Co_3O_4-A and (f) Co_3O_4-C.

many ultra-small interconnected/aggregated nanoparticles, demonstrating a typically hierarchical morphology. Bundles of porous nanorods with lengths in the range of micrometers are observed.

The features of the 3D hierarchical Co_3O_4 spheres were also confirmed by TEM. It can be seen that the obtained morphology concurs with the FE-SEM observations. At low magnification, the TEM images (Fig. 4b and e) demonstrate that bundles of nanorods are embodied in the Co_3O_4 structures. The insets in Fig. 4b and e further present the particle morphologies of the Co_3O_4 samples. The HR-TEM images shown in Fig. 4c and f confirm the unidirectional fringe patterns and thereby indicate the high crystalline nature of all the samples. The measured lattice fringe of 0.28 nm in Fig. 4c and f implies the presence of Co_3O_4 (220) crystal planes, as observed from the XRD results presented in Fig. 2a. The selected area electron diffraction (SAED) patterns (the insets of Fig. 4c and f) indicate polycrystalline nature of the hierarchical structure.

The irregular pores existing among the clustered Co_3O_4 particles induce the mesoporous structure. Nitrogen sorption isotherms were measured to gain information about the pore sizes and specific surface areas of the Co_3O_4 samples. Fig. 5 shows the adsorption–desorption isotherm and the Barrett–Joyner–Halenda (BJH) pore-size-distribution plot. According to the IUPAC classification, the type-IV isotherms with distinct hysteresis loops can be attributed to type H3, which suggest the presence of mesopores. Such mesopores are ascribed to spaces among nanorods and the interparticle spaces caused by the stacking of the Co_3O_4 nanoparticles. The values of the specific BET surface area (S_{BET}) of Co_3O_4-A, Co_3O_4-B and Co_3O_4-C are determined to be 78.25, 74.34 and 83.65 $m^2\ g^{-1}$, respectively. Co_3O_4-C with the 3D hierarchical urchin-like sphere morphology presents a slightly higher S_{BET} than the other two. The S_{BET} of Co_3O_4-A with sparse nanorods bundles is higher than Co_3O_4-B with the complete sphere like morphology. The reduced particle size and homogenous distribution are the main reason for the increased BET surface area of the Co_3O_4-C sample. The pore size distributions for each sample are shown as the insets in Fig. 5a–c, indicating the formation of randomly distributed pores with dominant diameter of 2.74, 2.52 and 3.94 nm, respectively. The BJH pore size distributions of Co_3O_4-A and Co_3O_4-C are in good agreement with the TEM analysis (Fig. S4†). The high surface area provides an easy penetration of the electrolyte into active materials and appropriate Li ion diffusion lengths. The presence of mesopores can also effectively accommodate the volume expansion during the charge–discharge process. The electrochemical performance was evaluated by preparing coin-type half cells that employ

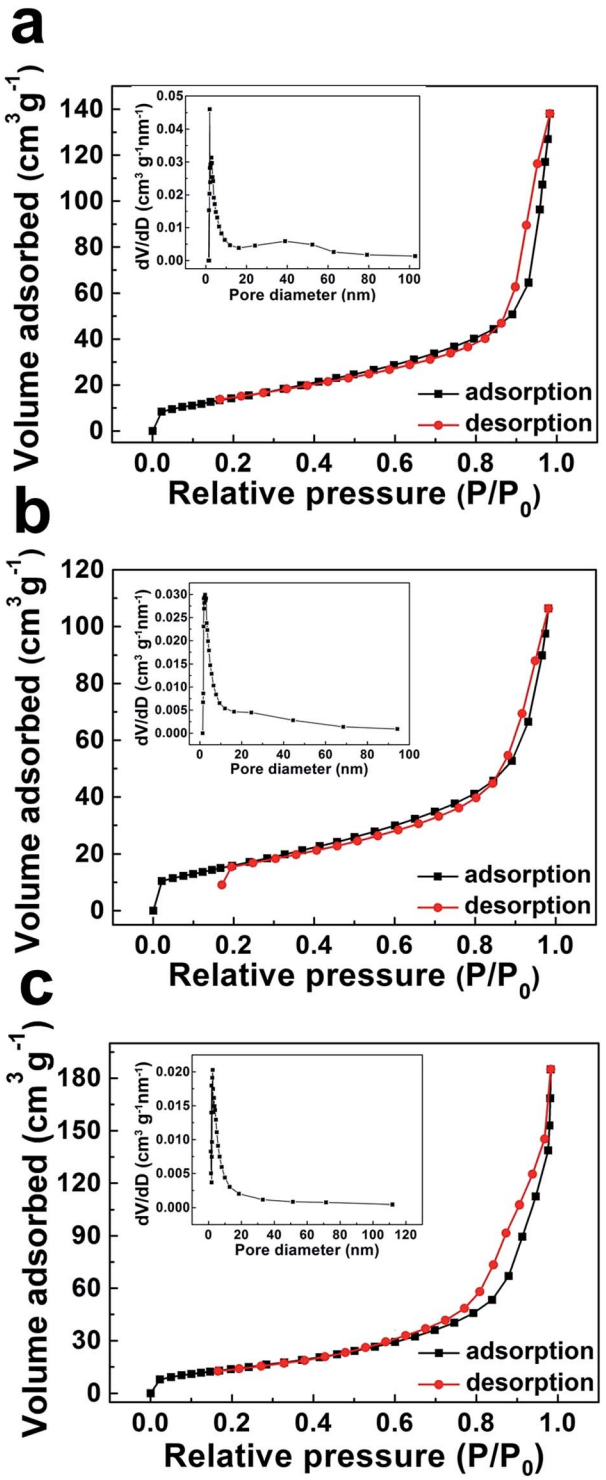

Fig. 5 Nitrogen adsorption–desorption isotherms and BJH pore size distribution plots (insets) of (a) Co_3O_4-A, (b) Co_3O_4-B and (c) Co_3O_4-C.

Co_3O_4 as the working electrode and Li foil as the counter/reference electrode.

The electrochemical performance of LIBs anode made from the 3D hierarchical Co_3O_4 spheres was evaluated by cyclic voltammetry (CV) and galvanostatic charge–discharge cycling. A cyclic voltammogram collected at a scan rate of 0.1 mV s^{-1} between 0.01 and 3.0 V is shown in Fig. 6a. In the first cycle, the small irreversible peak at around 1.0 V should be ascribed to lithium insertion into the crystal structure of the Co_3O_4 without structural change ($Co_3O_4 + xLi^+ + xe^- \rightarrow Li_xCo_3O_4$), and the latter sharp reduction peak located at 0.8 V is owing to the complete reduction of from Co^{x+} to Co(0) and the formation of a solid-electrolyte-interphase (SEI) layer. This reduction reaction has a significant effect on the reversible capacity of Co_3O_4.[37] The full lithiation voltage in the following cycles (about 1.1 V) is higher than that in the first cycle (about 0.8 V), probably due to the improved kinetics of the 3D hierarchical urchin-like Co_3O_4 electrode resulting from a microstructural alteration after the first lithiation. The improved kinetics may be due to inherent nanosize effects in the TMO electrode during the cycling. During the anodic polarization process, a broad peak at around 2.1 V is associated with the oxidation reactions and conversion of metallic cobalt into cobalt oxide. The overlapping of the CV curves in the subsequent cycles indicates good reversibility of the electrochemical reactions, and this is further confirmed by the following cycling performance test. The electrochemical reactions involved are presented as follows.[38,39]

$$Co_3O_4 + xLi \leftrightarrow Li_xCo_3O_4 \quad (1)$$

$$Li_xCo_3O_4 + (8 - x)Li \leftrightarrow 4Li_2O + 3Co \quad (2)$$

$$Co_3O_4 + 8Li^+ + 8e \leftrightarrow 4Li_2O + 3Co \quad (3)$$

Fig. 6b shows the galvanostatic charge–discharge curves of Co_3O_4-A, Co_3O_4-B and Co_3O_4-C under a current density of 200 mA g^{-1} within a voltage window of 0.01–3.0 V. For Co_3O_4-C electrode, no fading tendency in capacity is observed in the first 30 cycles. However, the capacity decreases after tens of cycles and is stable after 80 cycles. The reversible discharge capacity can remain as high as 1228 mA h g^{-1} after 170 cycles and larger than the theoretical one (890 mA h g^{-1}), suggesting excellent capacity retention. For comparison, Co_3O_4-A and Co_3O_4-B show a sharply decreasing trend in capacity, and only 452 and 351 mA h g^{-1} are retained after 100 cycles under the same conditions, respectively. The capacity lost in the first few cycles may attribute to the irreversible reactions involved in the formation of the SEI layer and the decomposition of electrolyte. As is well known, the formation and stabilization of the SEI layer is a gradual process, so that a growing coulombic efficiency gradually emerges, which is a typical phenomenon that has been described in many papers.[40–42] The increasing capacity of Co_3O_4-C electrode in the first 30 cycles may be due to an activation process caused by the enlarged surface area after a nanosize effect. However, the capacity decreases after tens of cycles, resulting from the deterioration of the hierarchical structure, which is an inherent characteristic for the TMO electrodes. The definitely superior performance of the Co_3O_4-C electrode may have resulted from the special 3D hierarchical urchin-like Co_3O_4 sphere structure.

Fig. 6c depicts the discharge–charge curves of Co_3O_4-C electrode for the selected cycles at a current density of

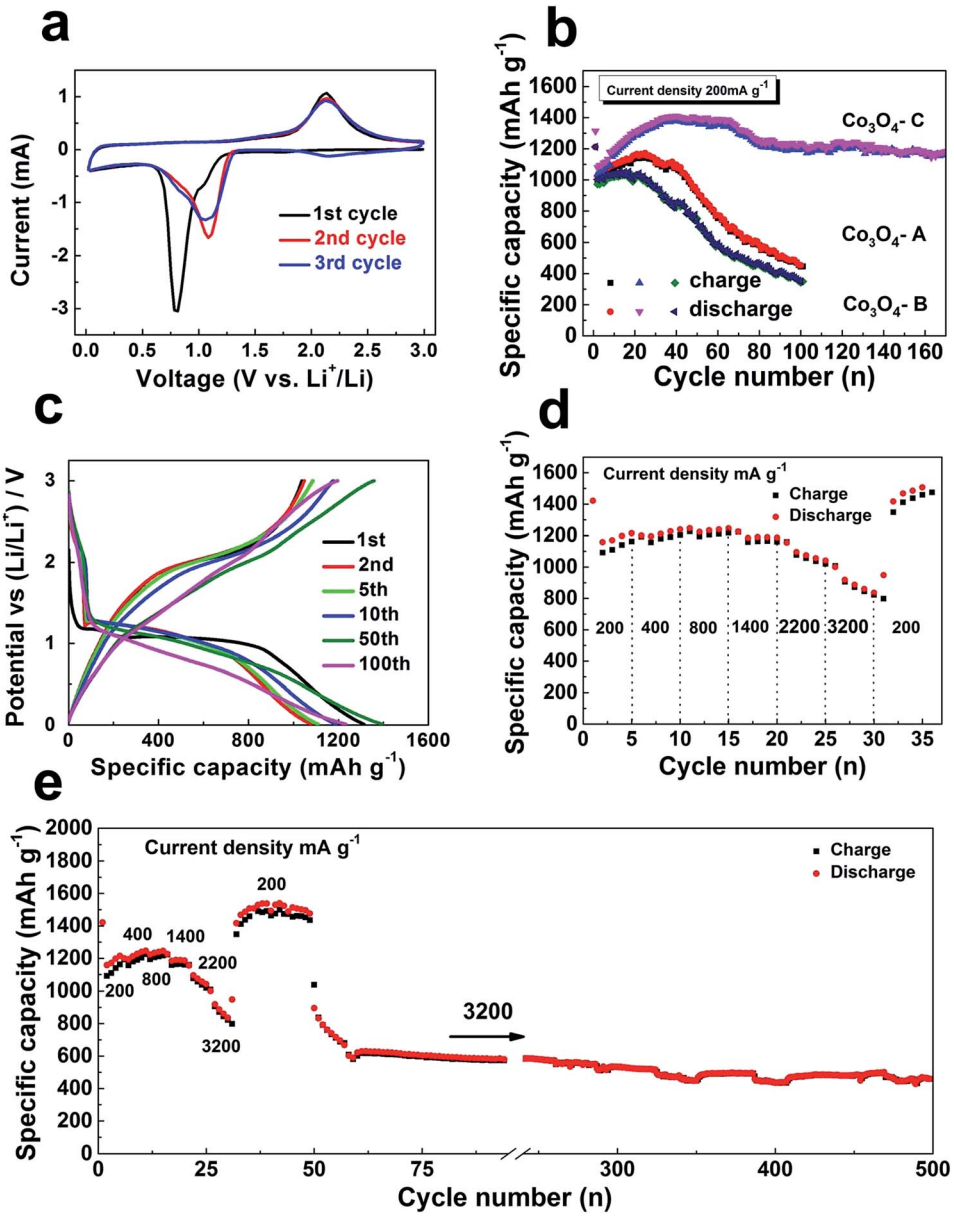

Fig. 6 (a) CV curves of Co_3O_4-C at a scan rate of 0.1 mV s^{-1} for the first three cycles; (b) cycling performance of Co_3O_4-A, Co_3O_4-B and Co_3O_4-C electrode at 200 mA g^{-1}; (c) charge–discharge curves for selected cycles of 3D hierarchical urchin-like Co_3O_4 electrode at 200 mA g^{-1}; (d and e) rate performance of Co_3O_4-C electrode.

200 mA g^{-1} with a cut off potential window of 0.01–3.0 V. The first discharge voltage profile displays a distinct discharge plateau at around 1.06 V followed by a gradual decrease to 0.01 V. The 3D hierarchical urchin-like Co_3O_4 electrode shows a high initial discharge capacity of 1314 mA h g^{-1} and charge capacity of 1038 mA h g^{-1}, resulting in a limited initial coulombic efficiency of 78.9%. The long stable voltage stage at about 1.06 V in the first discharge is ascribed to the complex phase transformation of Co_3O_4 to Co, the formation of SEI layer and the excess oxygen content in the material. Apart from the first cycle with a large irreversible capacity, subsequent cycles have a coulombic efficiency of almost 100%, which are shown in Fig. S5a–c.†

The rate performance of LIBs anode is very crucial, especially for high-power applications in power grids and electric vehicles. Fig. 6d and e shows the durable and stable rate capacity of the 3D hierarchical Co_3O_4 sphere at different current densities. When cycled at the current densities of 200, 400, 800, 1400, 2200 and 3200 mA g^{-1}, this electrode delivers discharge capacities of 1158, 1195, 1223, 1184, 1077 and 906 mA h g^{-1}, respectively (Fig. S6†). More importantly, a high capacity of 1407 mA h g^{-1} can be recovered rapidly when the current rate is reduced again from 3200 mA g^{-1} to 200 mA g^{-1}. The recovery of the capacity after extensive cycling at aggressive current implies that the electrode is not damaged and the integrity of the electrode is maintained during cycling process. When the current density

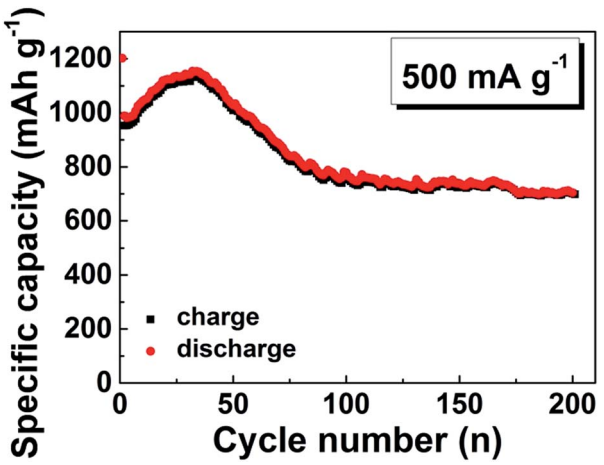

Fig. 7 Cycling performance of Co_3O_4-C electrode at 500 mA g^{-1}.

returns to 200 mA g^{-1} after 50 cycles, the discharge capacity of 1490 mA h g^{-1} can be still maintained, showing excellent rate capability. When the same cell is further cycled at an aggressive current (3200 mA g^{-1}), the capacity remains stable at 587 mA h g^{-1}, as is shown in Fig. 6e. The excellent electrochemical performance of the 3D urchin-like Co_3O_4 is due to its unique structural features. The mesoporous in spheres can effectively buffer the volume expansion during charge–discharge process and alleviate the pulverization of the electrode materials, hence improve the cycling stability. The electrode was separated from the collector at the fully charge state after 50 cycles. And then characterized by SEM, shown in Fig. S7.† The anode material maintains a sphere structure after 50 cycles, it reveals the excellent structural stability of the Co_3O_4.

To further characterize the cycling stability of the 3D hierarchical urchin-like Co_3O_4 electrode, cycling tests were performed at a current rate of 500 mA g^{-1} under ambient conditions. Fig. 7 shows the galvanostatic charge–discharge curves of the cell up to 200 cycles. The tendency is inconsistent with that observed in the cycling at 200 mA g^{-1}. In the initial eighty cycles, the capacity first increases and then decreases. The capacity of 3D hierarchical urchin-like Co_3O_4 electrode stabilizes at about 820 mA h g^{-1} after 80 cycles, with a coulombic efficiency of almost 100% (Fig. S5d†).

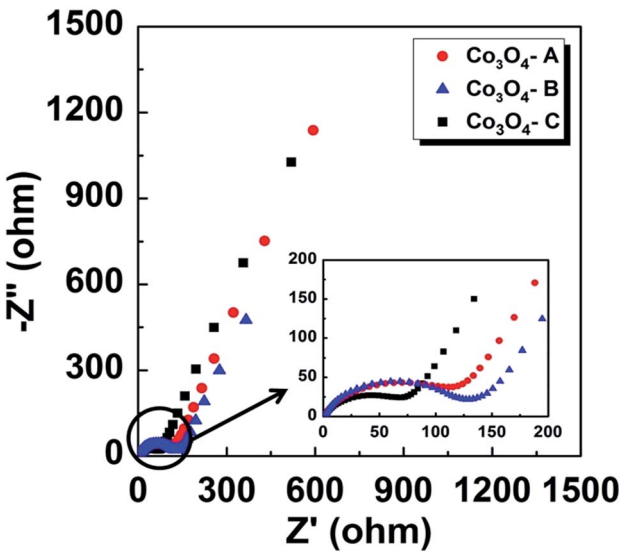

Fig. 8 Nyquist plots of different Co_3O_4 electrode materials in the frequency range between 100 Hz and 100 mHz.

Electrochemical impedance spectroscopy (EIS) was carried out to identify the charge transfer resistance in the electrode materials with various morphologies. Fig. 8 shows the EIS spectra of these three electrodes collected from fresh cells. The EIS curves exhibit a semicircular pattern in the high frequency region and a straight line in the low frequency region. Note that the diameter of the semicircle in the high-medium-frequency region for the 3D hierarchical urchin-like Co_3O_4 electrode (72 Ω) is smaller than that of the Co_3O_4-A and Co_3O_4-B electrode (115 Ω and 129 Ω), which demonstrates that the electrical conductivity and charge-transfer resistance are much smaller in the 3D hierarchical urchin-like Co_3O_4 electrode. It indicates that the 3D hierarchical urchin-like Co_3O_4 sphere provides efficient lithium diffusion tunnels and improves charge-transfer kinetics.

4. Conclusions

In summary, a series of 3D Co_3O_4 hierarchical microspheres have been successfully fabricated under various hydrothermal conditions. In contrast to Co_3O_4-A and Co_3O_4-B electrode, 3D hierarchical urchin-like Co_3O_4 spheres exhibits high reversible discharge capacity, excellent rate capability and good cycling performance when are used as LIBs electrode. The desirable electrode shows a stable reversible capacity of 1228 mA h g^{-1} after 170 cycles at 200 mA g^{-1} and high-rate performance with a capacity of 820 mA h g^{-1} after 200 cycles at 500 mA g^{-1}. More importantly, the reversible capacity of 587 mA h g^{-1} is observed after 500 cycles even at a high current density of 3200 mA g^{-1}. The unique 3D hierarchical urchin-like Co_3O_4 electrode facilitates lithium ion diffusion, prevents the collapse of the structure and improves charge-transfer kinetics during the charge–discharge cycling. The high electrochemical performance of 3D hierarchical urchin-like Co_3O_4 makes it a promising anode material for rechargeable LIBs.

Acknowledgements

This work is supported by NSFC (51472110, 11174112), Excellent Young and Middle-aged Scientists of Shandong Province (BS2014CL026) and Shandong Provincial Natural Science Foundation (JQ201214). The research programs from Ministry of Education, China, are also acknowledged (NCET-11-1027, 213021A). BC thanks the Taishan Scholar Chaired Professorship tenured at University of Jinan.

Notes and references

1 W. Tang, Y. S. Zhu, Y. Y. Hou, L. L. Liu, Y. P. Wu, K. P. Loh, H. P. Zhang and K. Zhu, *Energy Environ. Sci.*, 2013, **6**, 2093–2104.

2 W. Hao, S. Chen, Y. Cai, L. Zhang, Z. Li and S. Zhang, *J. Mater. Chem. A*, 2014, **2**, 13801–13804.
3 J. Jiang, Y. Y. Li, J. P. Liu, X. T. Huang, C. Z. Yuan and X. W. Lou, *Adv. Mater.*, 2012, **24**, 5166–5180.
4 W. W. Lee and J. M. Lee, *J. Mater. Chem. A.*, 2014, **2**, 1589–1626.
5 B. L. Ellis, P. Knauth and T. Djenizian, *Adv. Mater.*, 2014, **26**, 3368–3397.
6 P. Poizot, S. Laruelle, S. Grugeon, L. Dupont and J. M. Tarascon, *Nature*, 2000, **407**, 496–499.
7 C. Z. Yuan, H. B. Wu, Y. Xie and X. W. Lou, *Angew. Chem., Int. Ed.*, 2014, **53**, 1488–1504.
8 K. Z. Cao, L. Z. Jiao, H. Q. Liu, Y. C. Liu, Y. J. Wang, Z. P. Guo and H. T. Yuan, *Adv. Energy Mater.*, 2015, **5**, 1401421.
9 B. H. Zhou, S. L. Yang, L. D. Wu, W. Wu, W. F. Wei, L. B. Chen, H. B. Zhang, J. Pan and X. Xiong, *RSC Adv.*, 2015, **5**, 49926–49932.
10 D. H. Li, D. J. Yang, X. Y. Zhu, D. W. Jing, Y. Z. Xia, Q. Ji, R. S. Cai, H. L. Lia and Y. K. Che, *J. Mater. Chem. A*, 2014, **2**, 18761–18766.
11 B. Han, S. C. Zhang, R. Zhou, X. M. Wu, X. Wei, Y. L. Xing, S. B. Wang and T. Qi, *RSC Adv.*, 2014, **4**, 50752–50758.
12 J. S. Luo, X. H. Xia, Y. S. Luo, C. Guan, J. L. Liu, X. Y. Qi, C. F. Ng, T. Yu, H. Zhang and H. J. Fan, *Adv. Energy Mater.*, 2013, **3**, 737–743.
13 Z. L. Zhang, Q. Q. Tan, Z. Y. Zhong and F. B. Su, *RSC Adv.*, 2015, **5**, 40018–40025.
14 Y. N. Huang, C. C. Chen, C. H. An, C. C. Xu, Y. N. Xu, Y. J. Wang, L. F. Jiao and H. T. Yuan, *Electrochim. Acta*, 2014, **145**, 34–39.
15 J. Cabana, L. Monconduit, D. Larcher and M. R. Palacín, *Adv. Mater.*, 2010, **22**, E170–E192.
16 J. M. Xu, J. S. Wu, L. L. Luo, X. Q. Chen, H. B. Qin, V. Dravid, S. Mi and C. L. Jia, *J. Power Sources*, 2015, **274**, 816–822.
17 Y. Hou, J. Y. Li, Z. H. Wen, S. M. Cui, C. Yuan and J. H. Chen, *Nano Energy*, 2015, **12**, 1–8.
18 L. L. Jin, X. W. Li, H. Ming, H. H. Wang, Z. Y. Jia, Y. Fu, J. Adkins, Q. Zhou and J. W. Zheng, *RSC Adv.*, 2014, **4**, 6083–6089.
19 T. Yang, Y. A. Liu, Z. H. Huang, Q. Yang, M. Guan, M. H. Fang and X. W. Wu, *RSC Adv.*, 2015, **5**, 24486–24493.
20 B. Liu, X. B. Zhang, H. Shioyama, T. Mukai, T. Sakai and Q. Xu, *J. Power Sources*, 2010, **195**, 857–861.
21 H. Zhang, J. B. Wu, C. X. Zhai, X. Y. Ma, N. Du, J. P. Tu and D. R. Yang, *Nanotechnology*, 2008, **19**, 035711.
22 N. Du, H. Zhang, B. D. Chen, J. B. Wu, X. Y. Ma, Z. H. Liu, Y. Q. Zhang, D. R. Yang, X. H. Huang and J. P. Tu, *Adv. Mater.*, 2007, **19**, 4505–4509.
23 X. Chen, J. P. Cheng, Q. L. Shou, F. Liu and X. B. Zhang, *CrystEngComm*, 2012, **14**, 1271–1276.
24 N. Yan, L. Hu, Y. Li, Y. Wang, H. Zhong, X. Y. Hu, X. K. Kong and Q. W. Chen, *J. Phys. Chem. C*, 2012, **116**, 7227–7235.
25 X. Qing, S. Liu, K. Huang, K. Lv, Y. Yang, Z. Lu, D. Fang and X. Liang, *Electrochim. Acta*, 2011, **56**, 4985–4991.
26 D. W. Wang, Q. H. Wang and T. M. Wang, *Inorg. Chem.*, 2011, **50**, 6482–6492.
27 F. M. Zhan, B. Y. Geng and Y. J. Guo, *Chem.–Eur. J.*, 2009, **15**, 6169–6174.
28 J. S. Chen, T. Zhu, Q. H. Hu, J. Gao, F. Su, S. Z. Qiao and X. W. Lou, *ACS Appl. Mater. Interfaces*, 2010, **2**, 3628–3635.
29 X. Wang, H. Guan, S. M. Chen, H. Q. Li, T. Y. Zhai, D. M. Tang, Y. Bando and D. Golberg, *Chem. Commun.*, 2011, **47**, 12280–12282.
30 B. Yan, L. Chen, Y. J. Liu, G. X. Zhu, C. G. Wang, H. Zhang, G. Yang, H. T. Ye and A. H. Yuan, *CrystEngComm*, 2014, **16**, 10227–10234.
31 X. Y. Li, X. L. Huang, D. P. Liu, X. Wang, S. Y. Song, L. Zhou and H. J. Zhang, *J. Phys. Chem. C*, 2011, **115**, 21567–21573.
32 Y. H. Xiao, S. J. Liu, F. Li, A. Q. Zhang, J. H. Zhao, S. M. Fang and D. Z. Jia, *Adv. Funct. Mater.*, 2012, **22**, 4051–4058.
33 D. Q. Liu, X. Wang, X. B. Wang, W. Tian, Y. Bando and D. Golberg, *Sci. Rep.*, 2013, **3**, 2543–2548.
34 X. X. Zhang, Q. S. Xie, G. H. Yue, Y. Zhang, X. Q. Zhang, A. L. Lu and D. L. Peng, *Electrochim. Acta*, 2013, **111**, 746–754.
35 W. D. Shi, S. Y. Song and H. J. Zhang, *Chem. Soc. Rev.*, 2013, **42**, 5714–5743.
36 W. M. Mei, J. Huang, L. P. Zhu, Z. Z. Ye, Y. Mai and J. P. Tu, *J. Mater. Chem.*, 2012, **22**, 9315–9321.
37 K. J. Lee, T. H. Kim, T. K. Kim, J. H. Lee, H.-K. Song and H. R. Moon, *J. Mater. Chem. A*, 2014, **2**, 14393–14400.
38 W. Wen, J. M. Wu and M. H. Cao, *Nanoscale*, 2014, **6**, 12476–12481.
39 X. Huang, H. Yu, J. Chen, Z. Y. Lu, R. Yazami and H. H. Hng, *Adv. Mater.*, 2014, **26**, 1296–1303.
40 B. Wang, J. S. Chen, H. B. Wu, Z. Wang and X. W. Lou, *J. Am. Chem. Soc.*, 2011, **133**, 17146–17148.
41 N. Zhang, X. P. Han, Y. C. Liu, X. F. Hu, Q. Zhao and J. Chen, *Adv. Energy Mater.*, 2015, **5**, 1401123.
42 L. Zhang, H. B. Wu and X. W. Lou, *Mater. Horiz.*, 2014, **1**, 133–138.